

Portland State University

**PDXScholar**

---

Electrical and Computer Engineering Faculty  
Publications and Presentations

Electrical and Computer Engineering

---

10-18-2023

# Depth and Frequency Dependence of Geoacoustic Properties on the New England Mud Patch from reflection coefficient inversion

Jiang Yong-Min

*Center for Maritime Research and Experimentation*

Charles W. Holland

*Portland State University, hollan7@pdx.edu*

Stan E. Dosso

*University of Victoria*

Jan Dettmer

*University of Victoria*

Follow this and additional works at: [https://pdxscholar.library.pdx.edu/ece\\_fac](https://pdxscholar.library.pdx.edu/ece_fac)



Part of the [Electrical and Computer Engineering Commons](#)

**Let us know how access to this document benefits you.**

---


## Citation Details

Jiang, Y. M., Holland, C. W., Dosso, S. E., & Dettmer, J. (2023). Depth and frequency dependence of geoacoustic properties on the New England Mud Patch from reflection coefficient inversion. *The Journal of the Acoustical Society of America*, 154(4), 2383-2397.

This Article is brought to you for free and open access. It has been accepted for inclusion in Electrical and Computer Engineering Faculty Publications and Presentations by an authorized administrator of PDXScholar. Please contact us if we can make this document more accessible: [pdxscholar@pdx.edu](mailto:pdxscholar@pdx.edu).

OCTOBER 18 2023

# Depth and frequency dependence of geoacoustic properties on the New England Mud Patch from reflection coefficient inversion<sup>a)</sup> ✓

Yong-Min Jiang; Charles W. Holland; Stan E. Dosso ; Jan Dettmer



*J. Acoust. Soc. Am.* 154, 2383–2397 (2023)

<https://doi.org/10.1121/10.0021309>



View Online



Export Citation

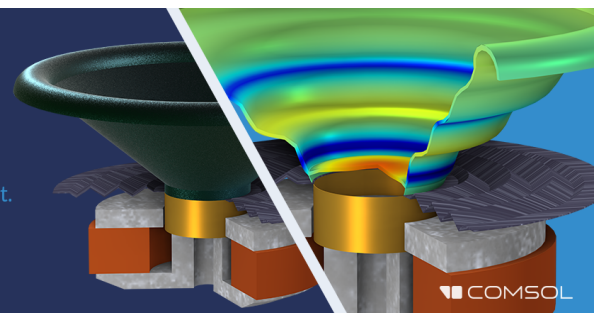
CrossMark




## Take the Lead in Acoustics

The ability to account for coupled physics phenomena lets you predict, optimize, and virtually test a design under real-world conditions – even before a first prototype is built.

» Learn more about COMSOL Multiphysics®



## Depth and frequency dependence of geoacoustic properties on the New England Mud Patch from reflection coefficient inversion<sup>a)</sup>

Yong-Min Jiang,<sup>1,b)</sup> Charles W. Holland,<sup>2</sup> Stan E. Dosso,<sup>1</sup>  and Jan Dettmer<sup>3</sup>

<sup>1</sup>*School of Earth and Ocean Sciences, University of Victoria, Victoria, British Columbia V8W 2Y2, Canada*

<sup>2</sup>*Department of Electrical and Computer Engineering, Portland State University, Portland, Oregon 97201, USA*

<sup>3</sup>*Department of Geoscience, University of Calgary, Calgary, Alberta T2N 1N4, Canada*

### ABSTRACT:

Muddy sediments cover significant portions of continental shelves, but their physical properties remain poorly understood compared to sandy sediments. This paper presents a generally applicable model for sediment-column structure and variability on the New England Mud Patch (NEMP), based on trans-dimensional Bayesian inversion of wide-angle, broadband reflection-coefficient data in this work and in two previously published reflection-coefficient inversions at different sites on the NEMP. The data considered here include higher frequencies and larger bandwidth and cover lower reflection grazing angles than the previous studies, hence, resulting in geoacoustic profiles with significantly better structural resolution and smaller uncertainties. The general sediment-column structure model includes an upper mud layer in which sediment properties change slightly with depth due to near-surface processes, an intermediate mud layer with nearly uniform properties, and a geoacoustic transition layer where properties change rapidly with depth (porosity decreases and sound speed, density, and attenuation increase) due to increasing sand content in the mud above a sand layer. Over the full frequency band considered in the new and two previous data sets (400–3125 Hz), there is no significant sound-speed dispersion in the mud, and attenuation follows an approximately linear frequency dependence. © 2023 Acoustical Society of America. <https://doi.org/10.1121/10.0021309>

(Received 20 June 2023; revised 23 August 2023; accepted 21 September 2023; published online 18 October 2023)

[Editor: Preston Scot Wilson]

Pages: 2383–2397

### I. INTRODUCTION

Geoacoustic properties of seabed sediments strongly influence acoustic propagation in shallow-water environments. Hence, approaches to estimate geoacoustic parameters and uncertainties and to understand and model sediment-acoustic interactions are important for underwater acoustics research and applications. Seabed geoacoustic properties are spatially variable both vertically and laterally, typically changing most rapidly with depth over the sediment column. Further, the compressional-wave (sound) speed and attenuation are frequency dependent (depending on sediment type), although discerning sound-speed dispersion and attenuation frequency dependence remains a challenging problem. Geoacoustic inversion, whereby seabed models are estimated from ocean acoustic data, represents an attractive remote-sensing alternative to direct (invasive) measurements for the study of *in situ* seabed properties and seismo-acoustic interactions.

Direct and acoustic methods have been applied extensively to investigate geoacoustic properties of the seabed in a variety of littoral environments, to quantify their acoustic behavior in various frequency bands, and to understand the

physical mechanisms that control sound propagation in different sediments.<sup>1–10</sup> Acoustic measurements vary greatly in terms of the lateral scale over which they sample the seabed, averaging over potential lateral variability (range dependence) of the environment. Some acoustic survey methods, such as single-bounce reflection measurements considered here,<sup>9–11</sup> insinuate a seafloor footprint of  $O(10^1)$  to  $O(10^2)$  m in lateral extent and can provide high-resolution estimates of the local depth-dependent structure, while others consider spatial scales of order  $O(10^3)$  to  $O(10^4)$  m, providing more regional averages. Further, various methods consider very different frequencies, varying from  $O(10^1)$  to  $O(10^6)$  Hz, with concomitant tradeoffs in spatial resolution and penetration depth.

Until recently, most of the work in acoustic data collection and geoacoustic inversion has been applied to study the properties and frequency dependence of sandy (granular) sediments, with a lack of equivalent attention paid to muddy (fine-grained) sediments, both theoretically and experimentally. To initiate and organize research efforts for fine-grained muddy sediments, the Office of Naval Research sponsored an international, multi-disciplinary sea-going research program on the New England Mud Patch (NEMP) in 2017, referred to as the 2017 Seabed Characterization Experiment (SBCEX17).<sup>12</sup> A number of different types of data were collected over a wide range of frequencies

<sup>a)</sup>This paper is part of a special issue on Assessing Sediment Heterogeneity on Continental Shelves and Slopes.

<sup>b)</sup>Email: minj@uvic.ca

(~10 Hz to 250 kHz) via direct measurements, short-range (~10–500 m) acoustic propagation experiments, and long-range (~0.5–10 km) propagation experiments.

One approach to acoustic data collection carried out as part of SBCEX17 involved short-range recordings of transient signals from a towed acoustic source at a bottom-moored hydrophone.<sup>11</sup> The recorded waveforms (time series) were processed as reflection coefficients over a range of seafloor-reflection angles and frequencies, providing high-information content data for geoacoustic inversion. These reflection measurements were collected at three sites on the NEMP. Two of the reflection-coefficient data sets, obtained with a surface-towed source, were considered previously by Belcourt *et al.*,<sup>13</sup> who applied trans-dimensional (trans-D) Bayesian inversion to estimate geoacoustic profiles, including sound speed and attenuation frequency dependence at thick- and thin-mud sites. The compressional-wave attenuation and details of the mud structure at these same two sites were considered in greater detail by Holland and Dosso.<sup>14</sup> In the present paper, a third data set is considered, which was collected at a thick-mud site using a deep-towed source that provided reflection-coefficient data at lower grazing angles and higher frequencies and over a larger bandwidth than the data considered previously. The results of this new inversion provide higher resolution and smaller uncertainties for geoacoustic profiles and frequency-dependence examination and are used here, together with the earlier two results, to construct a general interpretive model of the sediment-column structure and variability on the NEMP.

## II. EXPERIMENT AND DATA

### A. Study area and data collection

The SBCEX17 study area is located on the NEMP, a region of active fine-grained sediment deposition offshore Martha’s Vineyard, MA.<sup>15</sup> The study area is approximately 30 km (east–west) by 8 km (north–south) in size, between the 70 and 85 m isobaths, and corresponds to a muddy sediment “pond” where the seabed mud layer varies from about 3 to 12 m in thickness. Figure 1 shows a 2015 chirp sonar survey at the SBCEX17 study area in terms of two-way travel time (TWTT) to a seismic reflector identified as the base of the mud layer (interpolated from survey lines with ~250 m spacing).<sup>15</sup> This figure indicates that the mud thickness generally increases from the northwest to southeast. Core analyses indicate a relatively homogeneous mud layer, referred to as Unit 1, below which sand content increases in the mud (Unit 2), above a sand layer (Unit 3).<sup>16</sup> Unit 2 could be termed the geologic transition layer; however, in this paper, our interest is in the geoacoustic transition interval, defined as the depth interval where the sound speed is observed to increase substantially (due to the increase in sand). The geologic and geoacoustic transition intervals are not the same.<sup>14</sup> The transition interval, as discussed below, will always refer to the geoacoustic transition interval.

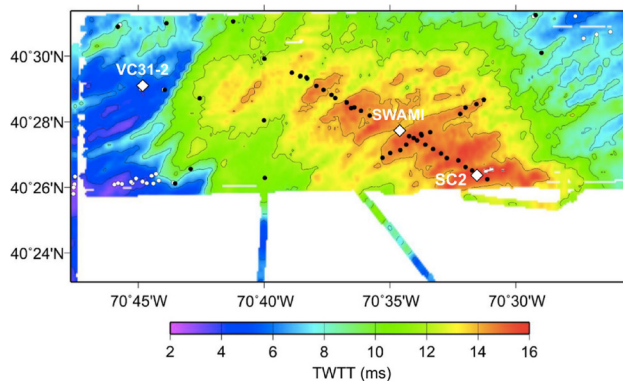


FIG. 1. (Color online) TWTTs to the mud-base reflector interpolated from a chirp sonar survey on the NEMP (Ref. 15), with three sites where wide-angle reflection-coefficient data were collected indicated by white diamonds. Black and white circles represent locations where piston cores and vibracores were collected, respectively.

Reflecting interfaces below the mud base (i.e., below the top of the sand layer) were also identified from the chirp survey. These are referred to as the deep-base I and deep-base II reflectors, but their geologic origins are unknown as no cores penetrated to the bottom of the sand layer, and the only cores that penetrated reliably to the top of the sand layer were at thin-mud sites (~3 m mud thickness).

In this paper, acoustic data collected at Site SC2 in the southeast of the SBCEX17 area are inverted for sediment properties, and the results are combined with those from previous geoacoustic inversions at Sites SWAMI and VC31-2<sup>13</sup> to develop a general model for the sediment-column structure at the NEMP. Figure 1 shows that TWTTs are similar at SC2 and SWAMI (thick-mud sites) and are significantly greater than at VC31-2 (a thin-mud site).

The acoustic data for SC2 were collected on April 3, 2017. Figure 2 illustrates the experiment geometry: An omnidirectional acoustic source (MC18) was towed by the RV *Neil Armstrong* at a depth of about 50 m and a speed of ~4 knots (2.1 m/s) along a radial survey track that passed within about 60 m of a bottom-moored hydrophone at ~66 m depth. The source transmitted a 1 s linear frequency-modulated pulse

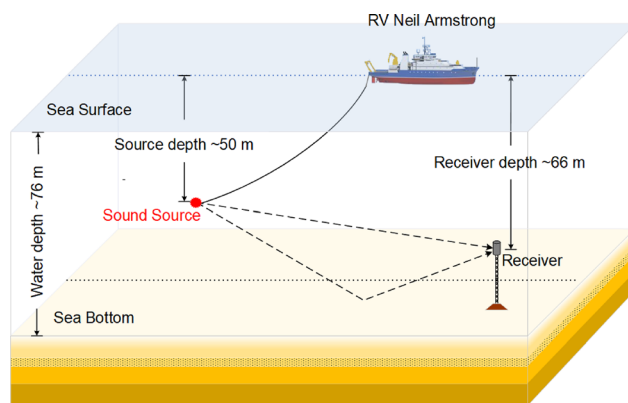


FIG. 2. (Color online) Data collection geometry. An omnidirectional acoustic source was towed at about 50 m depth along the survey track with acoustic arrivals recorded at a bottom-moored receiver at ~66 m depth.



over the frequency band 0.5–6.0 kHz at a 1 s repetition rate. The acoustic signals, including the direct arrival and reflections from the seafloor and sea surface, were recorded at the hydrophone with a sampling rate of 32 kHz. Additional details of the experiment can be found in Ref. 11. The water depth was relatively constant along the survey track at about 76 m, and conductivity-temperature-depth (CTD) casts indicated an essentially uniform water-column sound-speed profile with a seafloor value of 1472 m/s.

**B. Data processing**

Acoustic data processing and spherical-wave forward modeling (described in Sec. III A) require precise knowledge of the experiment geometry, including source and receiver depths, source–receiver range, and water depth at the seabed reflection point for each source transmission. To estimate high-precision geometric parameters, arrival times for direct, bottom-reflected, and surface-reflected paths were determined via cross correlation, and a ray-based, linearized Bayesian inversion was applied, regularized with a Gaussian prior for each parameter based on the best available information.<sup>17</sup> The grazing angles of seabed reflections were computed from the high-precision geometry estimates, and a Monte Carlo method was applied to compute grazing-angle uncertainties (based on drawing random realizations from the experiment-geometry uncertainty distributions<sup>17</sup>). Importantly, biases in the arrival times for the direct, bottom-reflected, and surface-reflected paths due to the source movement were not negligible in this analysis. Hence, Doppler effects were computed and compensated for all arrivals of each source transmission along the track, which significantly improved the geometric inversion and reflection-angle estimates.

Seabed reflection coefficients as a function of frequency for each source transmission (i.e., each seafloor-reflection angle) were computed using time-windowed direct and bottom-reflected arrivals, transformed to the frequency domain, accounting for geometric-spreading and absorption losses.<sup>9–11</sup> The bottom-reflected arrivals were time-windowed to capture all discernible reflecting horizons. This time window leads to a maximum bottom-interaction depth of ~17 m below the seafloor. Frequency averaging was applied over a 100 Hz band ( $\pm 50$  Hz) about each frequency. The resulting reflection coefficients are shown in Fig. 3. A frequency-dependent apparent critical angle (abrupt decrease in reflectivity with angle) is observed in Fig. 3 running from about 19° at 3.0 kHz to 23° at 0.5 kHz. Bragg oscillations in reflection-coefficient amplitude due to constructive/destructive interference within sediment layers are evident over most angles and frequencies.

The reflection-coefficient data chosen for geoacoustic inversion include seven center frequencies from 1175 to 2975 Hz (~1.34 octave band), with frequency averaging over  $\pm 50$  Hz, and grazing angles from 15.1° to 25.4°, as shown in Fig. 4 (this figure also includes predicted data from the geoacoustic inversion, described in Sec. IV A). The

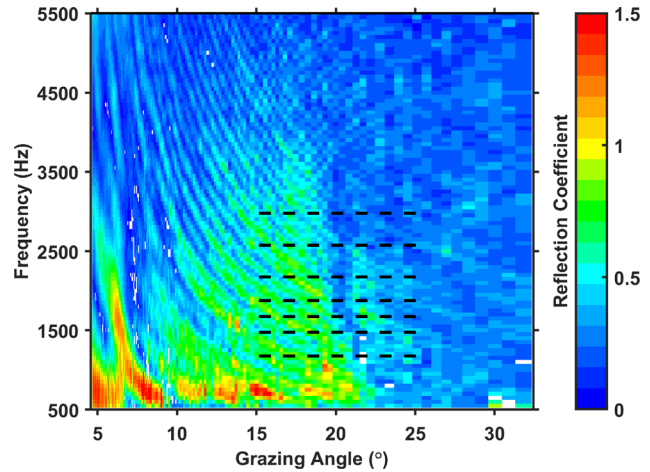


FIG. 3. (Color online) Seabed reflection coefficients as a function of grazing angle and frequency, averaged over 100 Hz frequency bands, computed from the recorded waveforms at Site SC2. Reflection coefficients at seven frequencies from about 1 to 3 kHz and angles from ~15° to 25° are used for inversion (dashed lines).

angles are unevenly spaced due to the experiment geometry and uniform source-tow speed, and the number of grazing angles differs slightly from frequency to frequency (23–27) due to the omission of low signal-to-noise ratio (SNR) results. The range of angles selected for inversion targeted data with high geoacoustic information content, including sub-critical and post-critical angle regimes. The frequency-dependent critical angle is highly informative, but the Bragg interference pattern is even more informative, yielding information on the depth and frequency dependence of sound speed and attenuation and the depth dependence of density in the mud layer. Relatively high frequencies were chosen as these are generally more informative since acoustic waves at smaller wavelengths sample sediment properties over more wave cycles within a layer. This is particularly true for attenuation, where more wave cycles lead to higher attenuation loss and higher sensitivity. Further, the relatively large total bandwidth, 1.8 kHz, permits multiple Bragg oscillations to be observed, which should, in theory, yield lower uncertainties. Larger bandwidths also provide a wider frequency range over which to detect sound-speed dispersion and attenuation frequency dependence in geoacoustic inversion results.

In terms of inverting for high-resolution geoacoustic profiles at a specific location, single-bounce reflection data have the advantage of a much smaller seafloor footprint, averaging over less lateral variability in the seabed, and are less sensitive to variability/uncertainty in the water-column sound-speed profile than acoustic data that involve continuous bottom interactions over multi-kilometer propagation ranges. For the reflection data set at SC2 (Fig. 4), the seabed is spatially averaged over a lateral distance of ~50 m, and the water column is laterally averaged over ~130 m.

The reflection-coefficient data set obtained here for Site SC2 differs in several ways from those at SWAMI and VC31-2 considered in previous work,<sup>13</sup> summarized in

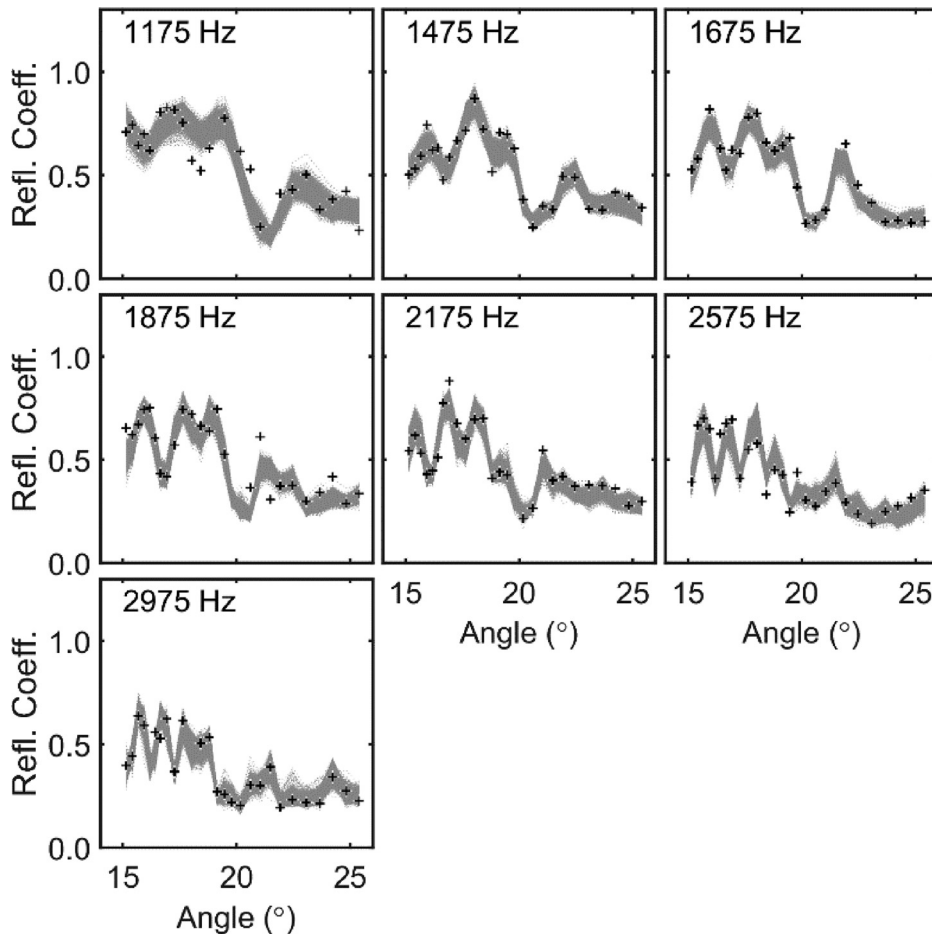


FIG. 4. Observed reflection-coefficient data used in the inversion represented by crosses and the ensemble of predicted data from inversion represented by gray distributions at the frequencies indicated.

Table I, due to different data collection procedures. While acoustic recordings at SC2 used a nearly omni-directional acoustic source towed at 50 m depth, recordings at SWAMI and VC31-2 used a directional source towed just below the sea surface (~0.4 m depth). Because of this, at SWAMI and VC31-2, the direct and surface-reflected arrivals could not be separated by time windowing (as at SC2), and the combination of the two was considered as a single arrival. While source directionality was estimated and accounted for in the data processing for SWAMI and VC31-2, the use of the omni-directional source at SC2 far from the sea surface leads to lower uncertainties in the measured reflection data. Further, the deep-towed source geometry at SC2 yields lower-angle data with acceptable SNR (in part due to shorter propagation paths), which are highly informative of sediment properties. Finally, the SC2 data set has roughly twice

the bandwidth (1175–2975 Hz) and more than an octave higher maximum frequency than the data at VC31-2 and SWAMI (frequency bands of 410–1362 and 410–1242 Hz, respectively).

### III. FORWARD AND INVERSE ALGORITHMS

This section summarizes the forward sediment-acoustic model (how sediment properties are parameterized), the forward acoustic reflection model (how the predicted reflection coefficients are computed), and the Bayesian inference method used for geoaoustic inversion.

#### A. Forward sediment-acoustic model

The sediment properties are parameterized using the viscous grain-shearing (VGS) sediment-acoustic model.<sup>18</sup>

TABLE I. Information summary for sites SC2, VC31-2, and SWAMI. The mud- and sand-base reflector depths are estimated using sediment sound speeds from inversions, and  $c_w$  represents the water sound speed at the base of the water column measured by CTD cast. Note that the angle ranges are those used in the inversions and do not represent the full range of angles collected.

Site	Receiver location		Water depth (m)	$c_w$ (m/s)	Frequency range (Hz)	Angle range (deg)	Mud-base depth (m)	Sand-base depth (m)
	Lat. (°N)	Lon. (°W)						
SC2	40.4400	-70.5269	76	1472.3	[1175, 2975]	[15, 25]	11.7	12.8
SWAMI	40.4614	-70.5753	76	1473.9	[410, 1242]	[25, 56]	10.3	11.5
VC31-2	40.4838	-70.7469	77	1470.9	[410, 1362]	[29, 60]	3.2	6.7

The VGS model was originally developed based on loss mechanisms that include grain-to-grain shearing, posited to be a nonlinear (strain-hardening) phenomenon, and fluid flow around the grains (classical viscosity). It might seem that the VGS model may not apply to mud since the underlying physics are ostensibly based on grain-to-grain shearing, whereas in cohesive muddy sediments, clay platelets are held together by electrochemical forces. However, if the attenuation frequency dependence is near  $f^1$  and the sound speed is independent of frequency (as observed for mud<sup>13</sup>), sediment losses are not due to classical viscosity, and the fundamental physics behind the VGS model reduce to the grain shearing (GS) model. Further, although the thinking behind GS invokes micro-roughness at granular sediment contacts, the actual physics and mathematics involve simple material impulse response functions intended to model the as-yet poorly understood micromechanics of grain-to-grain interactions. Ultimately, the physics of the GS model are implemented mechanistically as a Hookean spring and a strain-hardening dashpot. Given that the micromechanics of cohesive sediments are also poorly understood, the spring/strain-hardening dashpot model may be considered as somewhat general—applicable not only to grain-to-grain interactions, but also to other kinds of bonding.

One of the main advantages of using the VGS model is to ensure that the sound-speed dispersion and attenuation frequency dependencies do not violate causality. This ensures that parameter inter-dependencies, e.g., the frequency dependence of the sound speed and attenuation, are linked by the Kramers–Kronigs relations, which limit the solution space. Given these physical constraints, the inversion allows the data to determine the attenuation frequency dependence (which can vary between  $f^{1/2}$  and  $f^2$ ) and the associated sound-speed dispersion.

Our implementation<sup>19</sup> treats four parameters as depth independent and reasonably well known: the density and bulk modulus of the water and sediment grains. These are assigned narrow prior bounds to account for small uncertainties in the Bayesian inversion. The principal goal of the inversion is to estimate four depth-dependent parameters: porosity  $\phi$ , grain-to-grain compressional modulus  $\gamma_p$ , material exponent  $n$ , and compressional viscoelastic time constant  $\tau$ . The time constant controls dispersion characteristics. At infinitely small  $\omega\tau$  (where  $\omega = 2\pi f$  is the angular frequency), the attenuation goes as  $f^2$ , monotonically decreasing to  $f^1$  at  $\omega\tau = 1$  and then further decreasing to  $f^{1/2}$  at  $\omega\tau \sim 4$ ; for  $\omega\tau \lesssim 20$ , the attenuation is dominated by viscous losses. For  $\omega\tau \gtrsim 50$ , the attenuation goes as  $f^1$ . The sound-speed dispersion is likewise a strong function of  $\omega\tau$ , going as  $f^0$  at infinitely low frequency, increasing to a maximum rate of change at  $\omega\tau = 1$ , and then increasing log-linearly for  $\omega\tau \gtrsim 10$ . From these VGS parameters, the depth- and frequency-dependent sound speed and attenuation are computed as well as the depth-dependent density. In Sec. IV, both the VGS parameters and the corresponding properties of a fluid-sediment model (i.e., sound speed, density, attenuation) estimated from inversion are presented.

## B. Forward acoustic reflection model

Given the proximity of the source and receiver to the seafloor in the experiment geometry (Sec. II A), the plane wave approximation is not valid, and data prediction requires the computation of spherical-wave reflection coefficients. This is carried out by a numerical solution of the Sommerfeld integral, representing a plane wave expansion, over incident angle.<sup>20,21</sup> The integrand involves plane wave reflection coefficients, which are computed for multi-layer fluid-sediment models (calculated from VGS parameters) using a recursive algorithm.<sup>22</sup> For computational efficiency, the integral is evaluated using Levin integration,<sup>23,24</sup> with predicted data at all angles and frequencies computed in parallel on a graphics processing unit.<sup>21</sup>

## C. Trans-D Bayesian inversion

Trans-D Bayesian inversion is applied here to solve the combined problems of parameter estimation and model selection in the inversion of reflection-coefficient data. This approach has been described elsewhere<sup>21,25–27</sup> and is only summarized here. In a Bayesian approach, the goal of the inversion is the posterior probability density (PPD), defined as the (normalized) product of the prior probability density and the likelihood function. Here, bounded uniform priors are applied to all parameters, except for the number of seabed interfaces, where a Poisson distribution is also applied. The likelihood is based on the assumption of independent Gaussian-distributed errors, with standard deviations proportional to the magnitude of the observed data with an unknown error scale factor at each frequency. Specifically, for  $N$  data divided into  $N_D$  subsets and  $j = 1, \dots, N_i$  observed data  $d_{ij}$  in the  $i$ th subset (e.g., reflection-coefficient data at  $N_D$  frequencies with  $N_i$  angles at the  $i$ th frequency), the likelihood function is given by

$$L(\mathbf{m}, \mathbf{e}) = \frac{1}{(2\pi)^{N/2} \prod_{i=1}^{N_D} \prod_{j=1}^{N_i} e_i |d_{ij}|} \exp \left[ - \sum_{i=1}^{N_D} \sum_{j=1}^{N_i} \frac{|d_{ij} - d_{ij}(\mathbf{m})|^2}{2(e_i |d_{ij}|)^2} \right], \tag{1}$$

where  $d_{ij}(\mathbf{m})$  are predicted data for geoaoustic model  $\mathbf{m}$ , and  $e_i |d_{ij}|$  is the standard deviation for  $d_{ij}$  with  $e_i > 0$  representing the error scale factor at the  $i$ th frequency, and  $\mathbf{e} = \{e_i\}$  are the unknown error-model parameters included in the inversion.

The reversible-jump Markov-chain Monte Carlo (rjMCMC) algorithm<sup>28</sup> is applied to sample probabilistically over the choice of model parameterization (i.e., number of sediment interfaces) and corresponding parameters (interface depth and VGS parameters of the corresponding layers) plus the error-model parameters (scale factors). Efficient sampling, including a reasonable acceptance rate of dimension jumps (changes in number of interfaces), is achieved by a combination of parallel tempering<sup>27,29–31</sup> and principal-component reparameterization,<sup>27,32</sup> with parallel-tempering



chains run in parallel on a computer cluster of multiple central processing units. Once a large (convergent) sample of models is collected, and omitting the initial burn-in models during which stationary sampling is achieved, the number of interfaces is marginalized over in considering probabilistic results in terms of VGS or fluid-sediment model parameters. Statistical tests are applied to the data residuals (difference between observed and predicted data) *a posteriori* to validate the error-model assumptions.<sup>6</sup>

#### IV. INVERSION RESULTS AT SITE SC2

##### A. Trans-D inversion: Priors, data fit, sampling, and convergence

The trans-D Bayesian inversion algorithm described in Sec. III was applied to the observed reflection-coefficient data considered in Sec. II to estimate VGS parameters of the seabed sediments at Site SC2 on the NEMP. The priors for all parameters are summarized in Table II. Relatively wide prior bounds are assigned for the depth-dependent VGS parameters to allow the data to primarily determine the inversion results; three of these ( $\gamma_p$ ,  $n$ , and  $\tau$ ) are parameterized logarithmically in the inversion to account for potential variability over an order of magnitude or more. Depth-independent parameters are tightly constrained as these are generally well known (e.g., grain bulk density and bulk compressional modulus from Ref. 16). The number of parameters in the trans-D model varied from 16 to 76.

It should be noted that the grain bulk modulus is generally not measured (while reasonable measurements are available for the other three), but the grain bulk modulus is quite important for sound speed. In the VGS model, the sound-speed lower bound is set by the Mallock–Wood equation, which depends strongly on  $\kappa_g$ . Since the grain bulk modulus in some sediments may be smaller than that for a pure mineral (because of fractures within the grain and, for

clays, dependencies on temperature, pressure, ionic composition, and biological activity<sup>33</sup>), it follows that, for inversion,  $\kappa_g$  should be set to the lowest possible value, not the mean. The lowest possible value is not known. However, we estimate a reasonable global lower bound from the Mallock–Wood equation compared with an extensive set of *in situ* sound-speed measurements.<sup>34</sup> This ensures that the widest range of sediment properties can be considered in inversion, in that it prevents the sound speed from being biased toward high values. This does allow the possibility that the grain bulk modulus may be biased slightly low and the grain-grain compressional modulus slightly high compared to their actual *in situ* values, but, again, the sound speed will be unbiased. That is to say, the reflection-coefficient data have direct information about the sound speed, but indirect information on the coupled parameters of grain bulk modulus and grain-to-grain modulus.

Excellent agreement between the observed and predicted data is achieved in the inversion, as shown in Fig. 4. Sampling histories and marginal probability distributions for the log-likelihood (data fit) and the number of seabed interfaces sampled in the inversion are shown in Fig. 5. Approximately 400 000 samples were collected in the inversion after discarding the initial 80 000 samples as the burn-in phase; however, chain-thinning by a factor of 20 is applied for convenience in plotting figures in this paper. Figure 5 shows that a well-mixed Markov chain with a good acceptance rate for dimension changes was achieved. The most-probable number of seabed-layer interfaces is 11, with the distribution extending from 7 to 15. Sampling convergence was assessed by comparing marginal posterior probability profiles for geoacoustic parameters computed for the first and second halves of the ensemble of samples: The results were virtually identical, indicating the inversion results had ceased to change, and convergence was considered to be achieved. Examination of the estimated error statistics and underlying assumptions is presented in the Appendix.

##### B. Geoacoustic marginal probability profiles

Results of the geoacoustic inversion are shown in Fig. 6 in terms of marginal posterior probability profiles for interface depths and the depth-dependent VGS parameters; parameter estimates and uncertainties in terms of PPD means and 95% credibility interval (CI) widths are also given in Table III for porosity at selected depths (other parameters in the table are discussed later in this section). In Fig. 6, the plot bounds represent the prior bounds, and warm colors indicate high probabilities and cool colors low probabilities, with probabilities normalized independently at each depth for display purposes.

Of the four VGS parameters in Fig. 6, the sediment porosity  $\phi$  has the smallest uncertainties relative to its prior bound widths, consistent with its primary importance in defining sound speed and density values. Figure 6(b) indicates that the porosity decreases in two steps from a surficial

TABLE II. Parameter priors for Bayesian inversion, where bounds for base-model parameters are the same as for layer parameters, and  $N_F$  is the number of frequencies in the data set. Note that  $\gamma_p$ ,  $n$ , and  $\tau$  are parameterized logarithmically in the inversion, but linear values are given here.

Model parameter	Prior
Number of sediment layers $k$	[1, 16] + Poisson with $\lambda = 2$
<i>Depth-dependent (trans-D) parameters (<math>i = 1, \dots, k</math>):</i>	
Interface sub-bottom depth $h_i$	[0, 17] m
Porosity $\phi_i$	[0.15, 0.85]
Grain-to-grain compressional modulus $\gamma_{p_i}$	$[7.943 \times 10^6, 3.981 \times 10^8]$ Pa
Material exponent $n_i$	[0.0398, 0.3981]
Viscoelastic time constant $\tau_i$	[0.03, 50] ms
<i>Depth-independent parameters:</i>	
Fluid bulk modulus $\kappa_w$	$[2.2245, 2.2265] \times 10^9$ Pa
Fluid density $\rho_w$	[1.0263, 1.0267] g/cm <sup>3</sup>
Grain bulk modulus $\kappa_g$	$[2.00, 2.15] \times 10^{10}$ Pa
Grain density $\rho_g$	[2.47, 2.67] g/cm <sup>3</sup>
<i>Error-model parameters (<math>j = 1, \dots, N_F</math>):</i>	
Data error scale factors $e_j$	[0.001, 0.4]



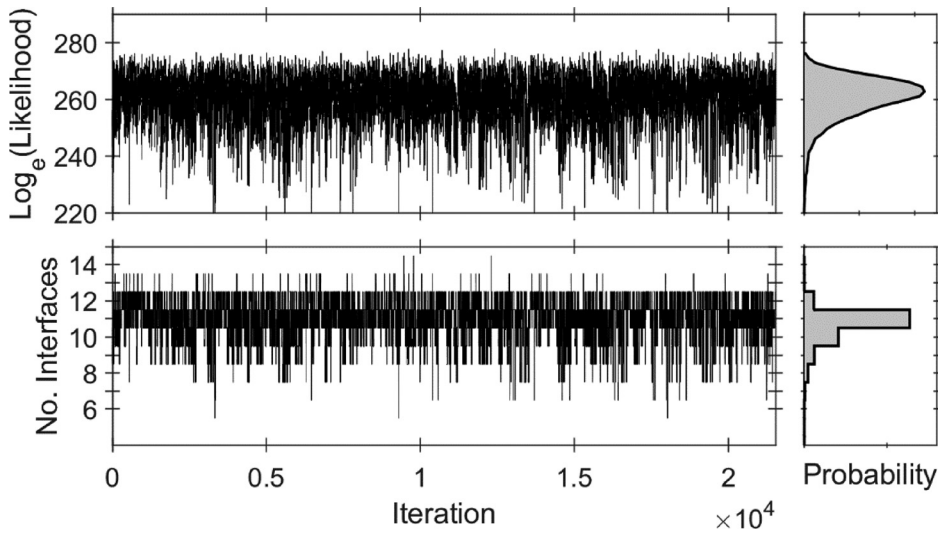


FIG. 5. Sampling histories and marginals for (upper row) data misfit and (lower row) number of interfaces in the trans-D sampling.

value of approximately 0.59 to 0.51 at about 2.4 m depth and then remains essentially constant to about 10.8 m, with some small fluctuations ( $\leq 0.1$ ) over the lower  $\sim 1.6$  m. From about 10.8 to 11.7 m depth, porosity decreases from  $\sim 0.49$  to 0.28 in two steps. From 11.7 to 12.8 m, porosity is about 0.29, and then it decreases to  $\sim 0.21$  for 12.8–14.4 m. Below 14.4 m, porosity appears to decrease slightly, although the significance of this is unclear given increased uncertainties. No further changes in porosity are observed above the  $\sim 17$  m basement (the maximum acoustic penetration given the time window applied in data processing). Porosity uncertainties, quantified in terms of 95%

CI widths, are about 0.02–0.04 from the surface to 14.4 m depth.

Interface depths in the marginal profile of Fig. 6(a) at  $\sim 11.7$ , 12.8, and 14.4 m were identified to represent the mud-base, sand-base, and deep-base I interfaces and agree closely (within 0.1–0.2 m) with the corresponding reflector depths computed using TWTTs interpolated from the chirp reflection survey<sup>15</sup> and sediment sound speeds from the inversion. The interpreted depths of the interfaces are included as dashed lines in Fig. 6. The significant decrease in porosity from 10.8 to 11.7 m depth corresponds to the sand-mud geoaoustic transition layer.

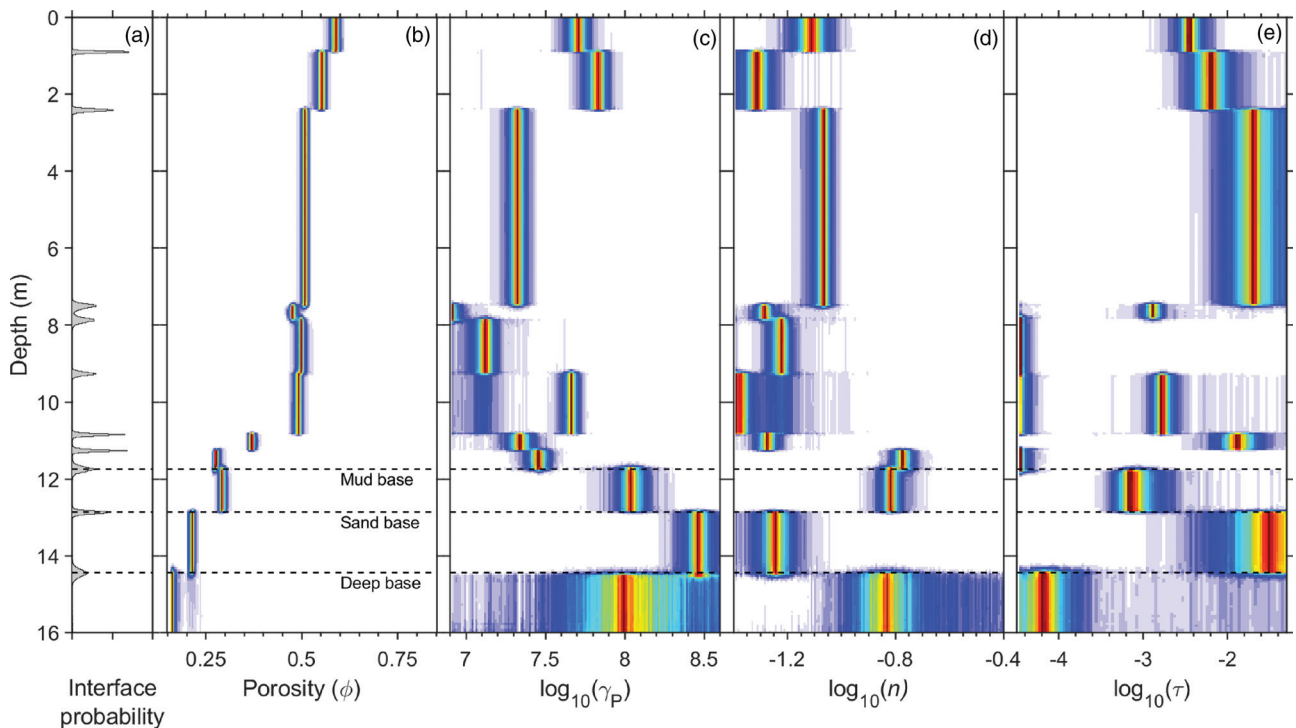


FIG. 6. Marginal posterior probability profiles for (a) interface depths and (b)–(e) VGS parameters porosity  $\phi$ , grain-to-grain compressional modulus  $\gamma_p$ , material index  $n$ , and compressional viscoelastic time constant  $\tau$ , respectively (last three parameterized logarithmically). Interpreted mud-base, sand-base, and deep-base I interfaces are indicated by dashed lines.

TABLE III. Mean parameter values and 95% CIs for porosity, sound speed, density, and attenuation at selected depths for Site SC2 ( $c_p$  and  $\alpha_p$  given for a frequency of 1175 Hz).

Depth (m)	$\phi$		$c_p$ (m/s)		$\rho_0$ (g/cm <sup>3</sup> )		$\alpha_p$ (dB/m/kHz)	
	Mean	CI	Mean	CI	Mean	CI	Mean	CI
0.5	0.586	[0.568, 0.604]	1466	[1462, 1470]	1.69	[1.65, 1.72]	0.08	[0.05, 0.14]
1.8	0.549	[0.525, 0.565]	1480	[1475, 1484]	1.75	[1.71, 1.79]	0.05	[0.03, 0.08]
4.0	0.507	[0.495, 0.520]	1488	[1484, 1492]	1.82	[1.79, 1.85]	0.03	[0.02, 0.04]
10.5	0.490	[0.468, 0.506]	1499	[1485, 1506]	1.84	[1.81, 1.88]	0.04	[0.02, 0.06]
11.0	0.369	[0.357, 0.382]	1589	[1574, 1597]	2.04	[2.00, 2.07]	0.01	[0.01, 0.03]
11.5	0.277	[0.263, 0.289]	1701	[1679, 1713]	2.19	[2.15, 2.21]	0.12	[0.08, 0.21]
12.5	0.292	[0.274, 0.306]	1735	[1729, 1741]	2.16	[2.12, 2.19]	0.42	[0.32, 0.50]
13.6	0.213	[0.201, 0.221]	1882	[1871, 1893]	2.29	[2.25, 2.31]	0.10	[0.07, 0.17]
15.2	0.174	[0.155, 0.234]	1969	[1928, 2013]	2.35	[2.24, 2.39]	0.89	[0.44, 1.74]

Given that the inversion algorithm applied here is based on uniform-layer models, some layered structure in the results could represent continuous gradients in the actual seabed sediments. In particular, the stepped porosity decreases from 10.8 to 11.7 m depth in Fig. 6(b) may represent a nonlinear negative gradient, as observed in fluid-sediment inversions of modal-dispersion data for the NEMP based on general gradient models.<sup>35</sup> Likewise, the stepped porosity decrease over the top 2.4 m could represent a negative gradient.

Figures 6(c)–6(e) show marginal profiles for VGS parameters corresponding to the grain-to-grain compressional modulus  $\gamma_p$ , material index  $n$ , and visco-elastic time constant  $\tau$ , respectively (parameterized logarithmically). Marginal profiles for all VGS parameters include a uniform layer from about 2.4 to 7.5 m in depth.

Inversion results in terms of fluid sediment-model parameters of sound speed  $c_p$ , bulk density  $\rho_0$ , and attenuation  $\alpha_p$  (in logarithmic units), computed from the VGS PPD, are shown in Fig. 7, including a zoom-in for sound speed over the top 4 m ( $c_p$  and  $\alpha_p$  are shown for a frequency of 1175 Hz, and the interface probability profile, mud-base, sand-base, and deep-base I interfaces are identical to those in Fig. 6). It should be noted that the thin layer between  $\sim 7.5$  and 7.9 m depth involving an abrupt change in attenuation (and other parameters in Figs. 5 and 6) seems unphysical and is likely an artifact of the data or inversion. Mean parameter estimates and 95% CI widths for these parameters are also given in Table III. The sound-speed results in Fig. 7(b) indicate a similar structure but opposite trends to the porosity in Fig. 6(b) (i.e., sound-speed increases correspond

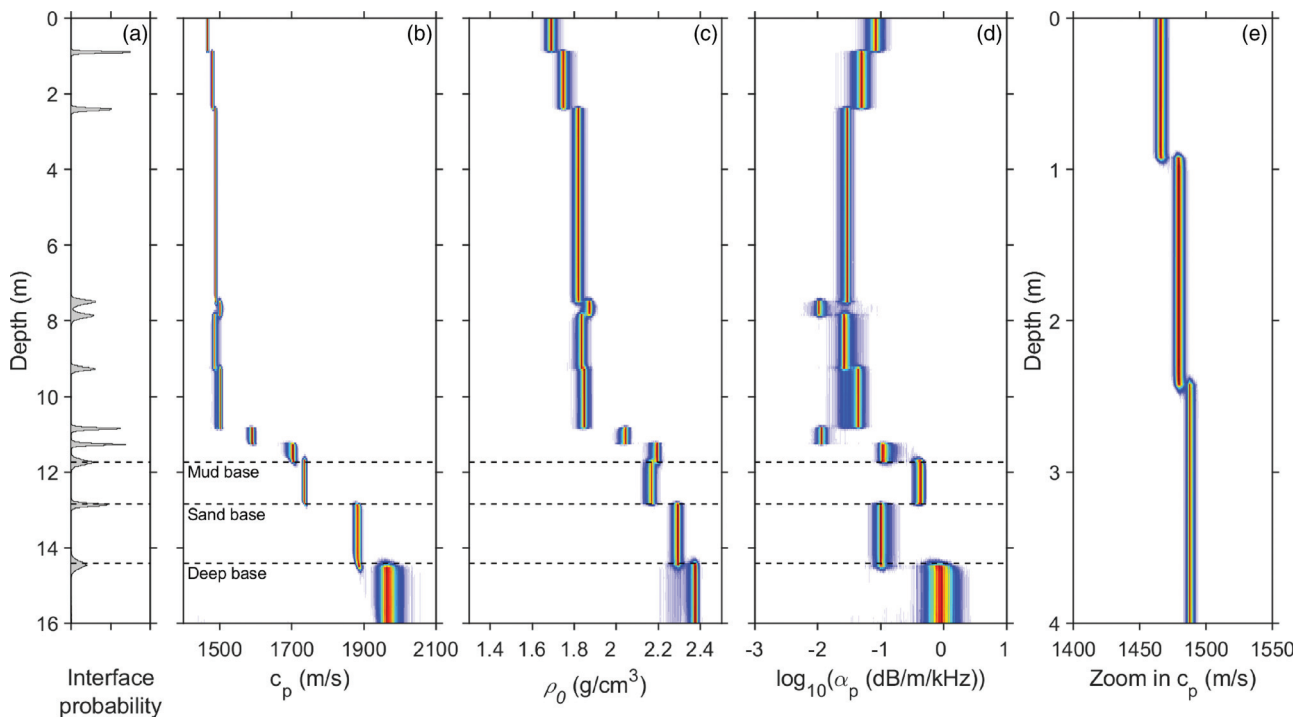


FIG. 7. Marginal posterior probability profiles for (a) interface depths and (b)–(d) geoaoustic parameters sound speed  $c_p$ , density  $\rho_0$ , and attenuation  $\alpha_p$ , respectively, with (e) showing a zoomed-in profile for  $c_p$  over the top 4 m (sound speeds and attenuations are shown for a frequency of 1175 Hz). Interpreted mud-base, sand-base, and deep-base I interfaces are indicated by dashed lines.

to porosity decreases and vice versa), due to their relationship in VGS theory. The average sound-speed gradient in the upper 4 m is  $\sim 6 \text{ s}^{-1}$ , below which there is an essentially iso-speed layer to about 10.8 m depth (with fluctuations and increasing uncertainty over the lower  $\sim 2.4$  m). From about 10.8 to 11.7 m, the sound speed increases from about 1499 to 1701 m/s, representing the sand-mud geoacoustic transition layer; below this are two layers with lower interfaces at about 12.8 m (sand-base) and 14.4 m (deep-base I) and sound speeds of  $\sim 1735$  and 1882 m/s, respectively. Below 14.4 m, a higher sound speed with large uncertainty is indicated. CI widths for sound speed vary from about 8 to 34 m/s over the top 14.4 m.

The density marginal profile in Fig. 7(c) shows a similar structure to the sound speed, with increases in density generally corresponding to increases in sound speed, and relatively small uncertainties: 95% CI widths vary from about 0.06 to 0.08  $\text{g/cm}^3$  to 14.4 m in depth. The attenuation profile in Fig. 7(d) is well determined, with CI widths varying from 0.02 to 0.18 dB/m/kHz to 14.4 m depth. The attenuation is observed to decrease from the surface to about 2.4 m depth. Although the mechanism for this decrease is not well understood, it is consistent with the two other sites (VC31-2 and SWAMI) at the NEMP<sup>13</sup> as well as direct measurements of attenuation in muddy sediments of the Eel River.<sup>36</sup> Below this, attenuation remains constant to about 7.5 m depth and then is variable but decreases slightly to 10.8 m. Over 10.8–11.7 m depth (the transition layer) the attenuation increases rapidly. Attenuation results are discussed further in Sec. V.

### C. Sound-speed dispersion and attenuation frequency dependence

In this section, the dispersion of sound speed and frequency dependence of attenuation for the seabed sediments at Site SC2 are investigated in a manner similar to earlier work at SWAMI and VC31-2.<sup>13</sup> Fig. 8 shows marginal probability densities for sound speed and log-attenuation computed from the VGS inversion results at frequencies from 1125 to 3125 Hz and for seven depths from 0.5 to 15.2 m selected to investigate specific features of the profile. These depths are the same as those considered in Table III for a frequency of 1175 Hz and are illustrated on the sound-speed and attenuation marginal profiles in Figs. 8(a) and 8(d), respectively.

Considering first sound-speed dispersion in the mud above the transition layer, Fig. 8(b) shows that at depths of 0.5, 1.8, and 4.0 m, there is no discernible increase in sound speed over the frequency band considered despite small uncertainties (95% CIs  $\leq 9$  m/s). At 12.5 m depth, in the sand layer, the mean sound speed increases by about 13 m/s from 1125 to 3125 Hz, with the sound-speed increase resolved beyond uncertainties. At 13.6 m depth, between the sand base and deep base, a smaller sound-speed increase ( $\sim 5$  m/s) may occur over this frequency band, but the difference is not resolved beyond uncertainties. At 15.2 m depth, below the deep base, a 50 m/s increase is suggested, but not resolved beyond the large uncertainties.

Considering next the attenuation frequency dependence, Fig. 8(c) shows no discernible change (less than 0.002

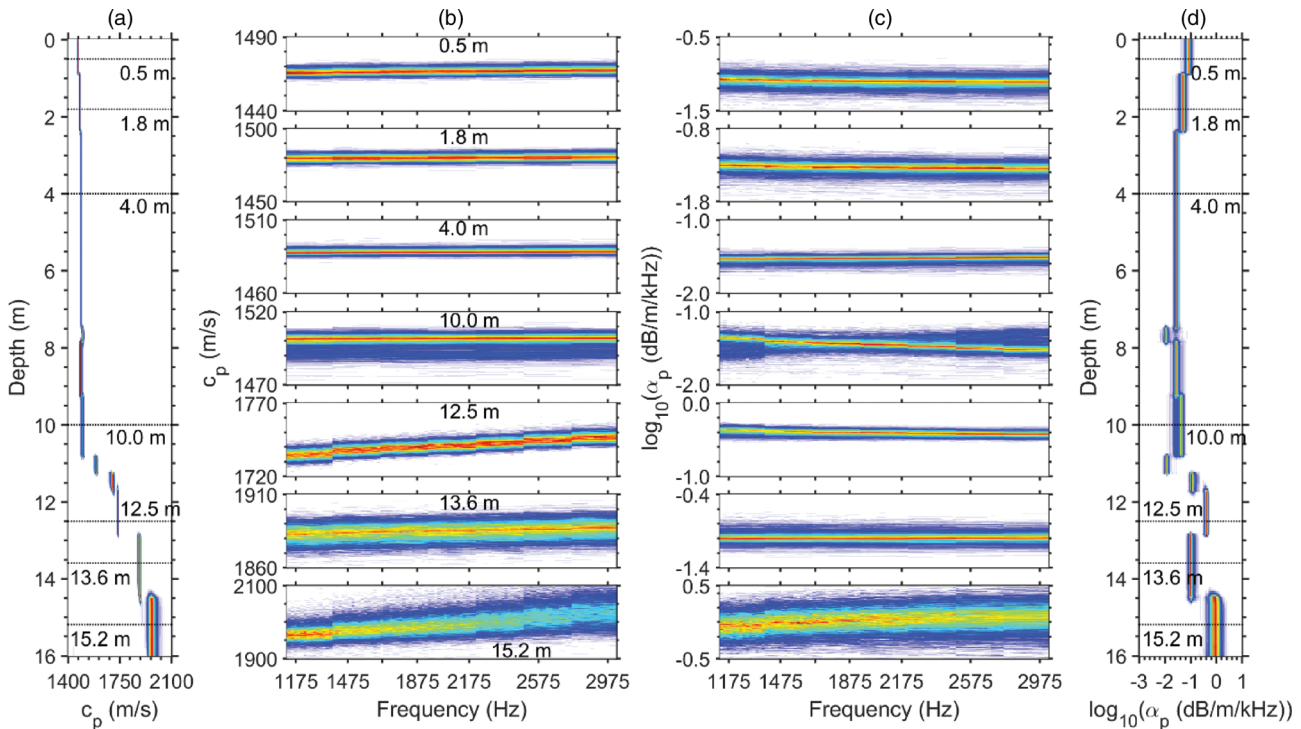


FIG. 8. (a) and (d) Sound-speed and attenuation marginal probability profiles indicating selected depths where sediment frequency dependence is considered (dotted lines with depths given), respectively. (b) and (c) Marginal PPDs for sound-speed dispersion and attenuation frequency dependence, respectively, at the selected depths. Note that the ordinate range for all sound-speed plots in (b) is 50 m/s except at 15.2 m depth, where it is 200 m/s, and the ordinate range is 1 for all log-attenuation plots in (c).

dB/m/kHz) in attenuation over the frequency band for mud depths of 0.5, 1.8, and 4.0 m. At 10.0 m depth (bottom of the iso-speed mud section), a small decrease in attenuation ( $\sim 0.015$  dB/m/kHz) is indicated. This is caused by the low values at this depth in the bi-modal distribution for the viscoelastic time constant  $\tau$ , shown in Fig. 6(e), which are likely unrealistic. The relatively large uncertainties in the frequency-dependent attenuation and sound-speed dispersion estimates at 10.0 m are due to the combination of the bi-modal distribution for  $\tau$  and the larger uncertainties for  $\gamma_p$  and  $n$  from 9.3 to 10.8 m depth. In and below the sand layer, no significant change in attenuation is indicated. For attenuation expressed here in units of decibels per meter per kilohertz, a constant value (or constant log value) is equivalent to a first-power frequency dependence ( $f^1$ ) over the 1125–3125 Hz band.

### V. SEDIMENT STRUCTURE AND VARIABILITY AT THE NEMP

This section considers the new inversion results for Site SC2 together with previous results at SWAMI and VC31-2<sup>13</sup> in constructing a general model of the sediment-column structure and in investigating spatial variation at the NEMP. Results at the three sites were all obtained via trans-D inversion of reflection-coefficient data, employing the VGS sediment model and spherical-wave data predictions. However, there are differences in the angular range and frequency band of the data sets (Table I), such that information content differs between sites.

Figure 9(a) provides an interpreted model representing sediment-column structure on the NEMP for a mud thickness corresponding to that at Site SC2, but believed to be generally applicable (with some variability) across the mud patch. This model is based on information from the reflection-coefficient inversion results at the three sites as well as core measurements<sup>16</sup> and the chirp sonar survey.<sup>15</sup> Figs. 9(b)–9(d) show sediment sound-speed profiles from the inversions at the three sites in terms of PPD mean estimates and 95% CI uncertainties, arranged so that the top of the sand-mud transition layer aligns across all panels. In the interpretation of Fig. 9(a), the mud consists of three layers: an upper layer roughly 4 m thick in which properties vary slightly with depth due to near-surface processes such as bioturbation; an intermediate layer with uniform properties that extends to about 1–2 m above the mud base; and a sand-mud transition layer in which geoacoustic properties change rapidly with depth due to increasing sand content in the mud. The transition layer terminates at the mud-base interface, below which is a layer of sand. Below the sand layer (sand-base interface) is the deep-base I interface.

The sound-speed inversion results at the three sites in Figs. 9(b)–9(d) correspond to the general structure in Fig. 9(a), with some differences between sites due to geographic variation and possibly due to differences in data information content. In consideration of the latter, note that the reflection-coefficient data at SC2 are expected to be the most informative (see discussion in Sec. II), and the inversion results at SC2 do indeed provide the best resolution and

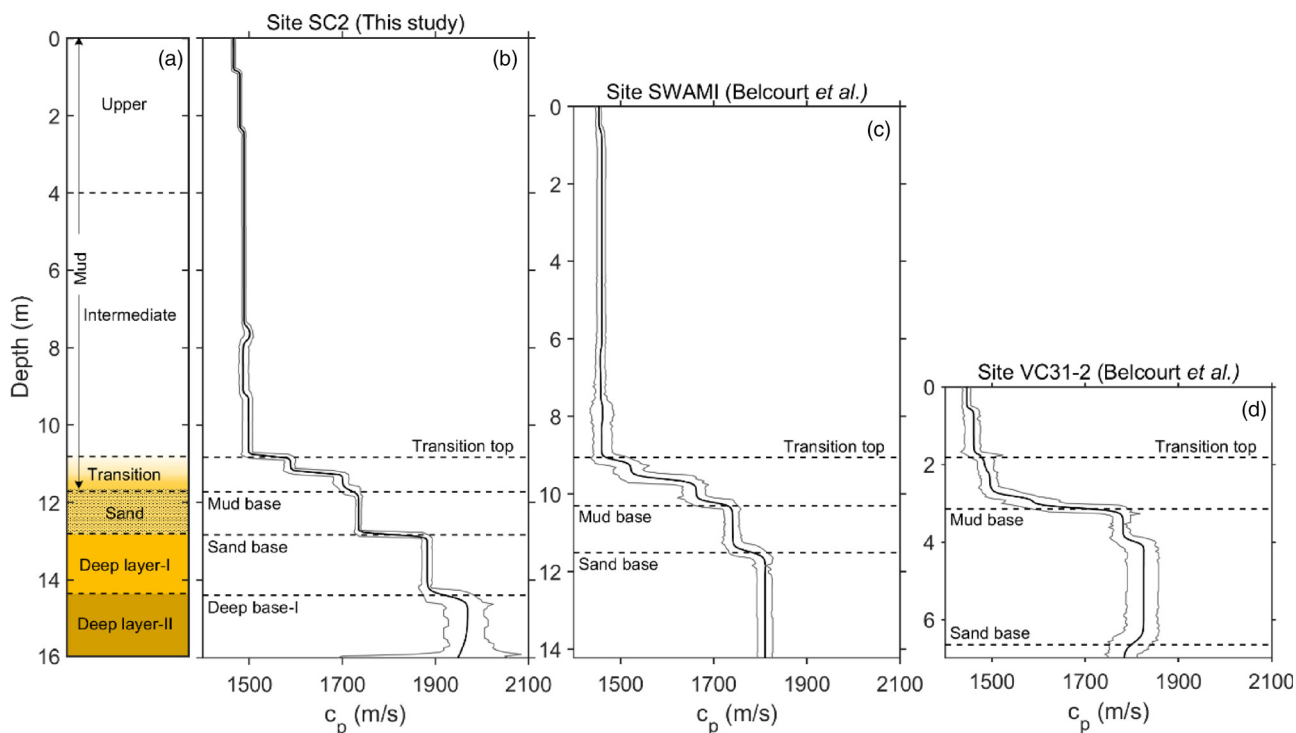


FIG. 9. (Color online) (a) Interpreted model of the sediment-column composition at the NEMP (explained in text). (b)–(d) Sound-speed inversion results at Sites SC2 (at 1175 Hz), SWAMI (1081 Hz), and VC31-2 (1081 Hz), respectively, with the latter two calculated from the VGS models presented in Ref. 13. Solid curves indicate mean sound-speed profiles, and gray curves are 95% CIs. Horizontal dashed lines indicate the depths (from top down) of the top of the transition layer, the mud base, the sand base, and, at SC2, deep-base I.



smallest uncertainties for sediment structure. Figure 9 shows that the total thickness of the mud, from the seafloor to the mud base, decreases from  $\sim 11.7$  m at SC2 to 10.3 m at SWAMI to 4.0 m at VC31-2, in close agreement with the chirp sonar results. At all sites, the upper mud layer is characterized by low surficial sound speeds of 1446–1466 m/s and a small increase in sound speed with depth. The intermediate mud layer, characterized by an essentially constant sound speed  $< 1500$  m/s, extends to about 10.8 m depth at SC2 and 9 m at SWAMI but is essentially absent at the thin-mud site VC31-2, where the upper layer extends to the top of the transition layer at about 2 m depth. At all sites, the transition layer is characterized by a rapid increase in sound speed through a series of steps (or a gradient), changing from  $< 1500$  m/s to about 1700–1740 m/s. The transition layer is reasonably consistent in thickness: about 0.9 m at SC2 and 1.3 m at the other two sites. Below this transition, the thickness of the sand layer is  $\sim 1.1$  m at SC2 and SWAMI and  $> 3$  m at VC31-2. The sound speed in the sand varies from  $\sim 1740$  m/s at SC2 and SWAMI to  $\geq 1800$  m/s at VC31-2 (but with large uncertainties). Below the sand layer, the deep-base I interface is resolved at SC2 as a significant increase in sound speed (and uncertainty) but is not observed in the inversion results for the other two sites.

To further compare sediment properties at the three sites, Fig. 10 shows marginal probability densities for porosity, sound speed, and log-attenuation in the upper mud layer at 0.1 m depth and in the sand layer at depths appropriate to each site (5 m at VC31-2, 10 m at SWAMI, and 12.5 m at

SC2). Results for the sound-speed ratio between the mud at 0.1 m depth and seawater at the base of the water column are also included in the figure. In each panel of Fig. 10, the sites are arranged from top down, corresponding to a progression from northwest to southeast on the NEMP (Fig. 1). PPD mean estimates and 95% CI uncertainties for these properties are tabulated in Table IV.

Figure 10 and Table IV show that uncertainties for the new results for SC2 are significantly smaller than those for the other two sites. Considering first the results at 0.1 m depth in the mud, there appears to be a trend with porosity decreasing, and sound speed and sound-speed ratio increasing, from the northwest to southeast. These trends are consistent with (but not informed by) northwest to southeast trends of increasing mean grain size and increasing sand content in near-surface core samples.<sup>16</sup> The increase in sound-speed ratio from northwest to southeast was also observed in high-frequency measurements obtained using the Sediment Acoustic-speed Measurement System probe.<sup>37</sup> In Fig. 10, the sound-speed ratio is less than unity (by an amount greater than the uncertainty) at all sites. In the sand, there is no definitive evidence, given uncertainties, of variation in porosity between sites, although CIs suggest the possibility of a decrease from northwest to southeast. The sand sound speed and attenuation appear to be highest at VC31-2, where the sand layer is thickest, while sand sound speed is similar at SWAMI and SC2.

Most published geoacoustic inferences at the NEMP treat the entire mud layer as a single unit and report the

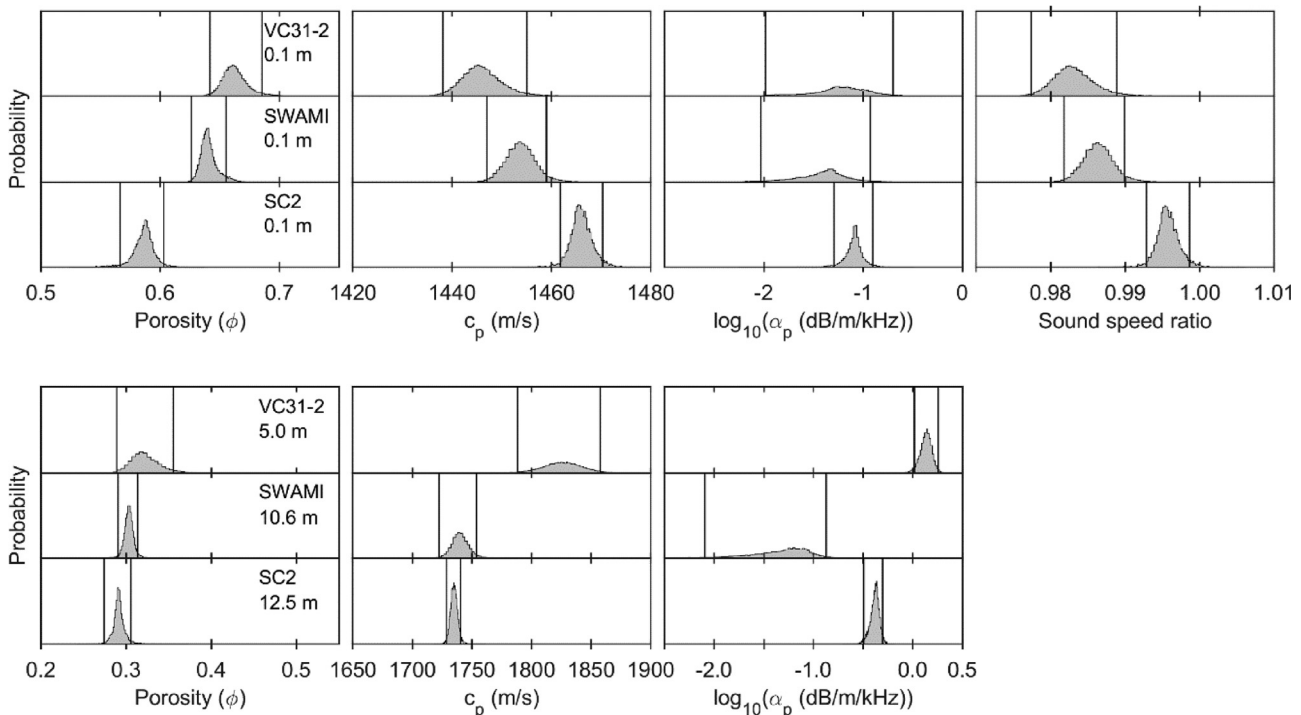


FIG. 10. Marginal probability densities for selected sediment properties at sites VC31-2, SWAMI, and SC2 from top down in each panel (a northwest to southeast progression at the NEMP). Columns of panels, from left to right, show results for porosity, sound speed, log-attenuation, and sound-speed ratio. Rows of panels, from top down, show results for the upper mud at 0.1 m depth and for the sand layer at depths appropriate to each site as indicated. Vertical lines delineate 95% CIs. Sound speeds and log-attenuations are for frequencies of 1181 Hz for VC31-2 and SWAMI and 1175 Hz for SC2.

TABLE IV. Mean parameter estimates and 95% CIs in mud at 0.1 m depth and in the sand layer at appropriate depths for sites VC31-2 (1081 Hz), SWAMI (1081 Hz), and SC2 (1175 Hz).

At water/sediment interface (0.1 m in sediment):									
Site	Depth (m)	$\phi$		$c_p$ (m/s)		$\alpha_p$ (dB/m/kHz)		Sound-speed ratio	
		Mean	CI	Mean	CI	Mean	CI	Mean	CI
VC31-2	0.1	0.66	[0.64, 0.69]	1446	[1438, 1455]	0.06	[0.01, 0.20]	0.983	[0.977, 0.989]
SWAMI	0.1	0.64	[0.63, 0.66]	1454	[1447, 1459]	0.04	[0.01, 0.12]	0.986	[0.982, 0.990]
SC2	0.1	0.59	[0.57, 0.60]	1466	[1462, 1470]	0.08	[0.05, 0.12]	0.996	[0.993, 0.999]

In sand layer:									
Site	Depth (m)	$\phi$		$c_p$ (m/s)		$\alpha_p$ (dB/m/kHz)		Sand layer thickness (m)	
		Mean	CI	Mean	CI	Mean	CI	Mean	CI
VC31-2	5.0	0.32	[0.29, 0.36]	1826	[1788, 1858]	1.36	[1.04, 1.80]	3.5	[3.2, 3.8]
SWAMI	10.6	0.30	[0.29, 0.31]	1741	[1722, 1754]	0.05	[0.01, 0.13]	1.3	[1.1, 1.5]
SC2	12.5	0.30	[0.27, 0.31]	1735	[1729, 1741]	0.41	[0.32, 0.50]	1.1	[1.0, 1.3]

depth-averaged attenuation. In Ref. 14, a simple model was proposed to predict the mud unit depth-averaged attenuation that assumes:

- (1) The attenuation above the transition interval is more or less uniform across the NEMP with a depth-interval average of 0.025 dB/m/kHz,
- (2) The attenuation in the transition interval is more or less uniform across the NEMP with a depth-interval average of 0.017 dB/m/kHz,
- (3) The transition interval has approximately the same thickness across the NEMP at 1.2 m.

Thus, the only input to this model is mud thickness. The model<sup>14</sup> predicted the depth-averaged attenuations at the thin- and thick-sediment sites (VC31-2 and SWAMI), which differ by a factor of 2, as well as the depth-averaged attenuation obtained by Knobles *et al.*<sup>38</sup> and Wan *et al.*<sup>39</sup> in a thick-sediment area. The new results at SC2 provide another opportunity to test that model. With a mud thickness of 11.7 m, the model predicts a depth-averaged attenuation of 0.040 dB/m/kHz. The measured depth-averaged attenuation, i.e., averaging over the depth-dependent results (the fourth column of Fig. 7), is 0.041 dB/m/kHz at 1175 Hz. Since attenuation is observed to be a nearly linear function of frequency, i.e., nearly constant with frequency in units of dB/m/kHz, the proposed model appears reasonable at this site as well.

## VI. SUMMARY AND DISCUSSION

Wide-angle reflection-coefficient data are highly informative for sediment properties and have been applied in geoacoustic inversion for various sediment types in shallow-water environments.<sup>7-9,13,14,21</sup> This paper applied trans-D Bayesian inversion, a VGS sediment-acoustic model, and a spherical-wave forward model to reflection-coefficient data collected at a thick-mud site (SC2) on the NEMP, with a focus on exploring geoacoustic properties and frequency

dependencies in greater detail and for higher frequencies than considered previously. In particular, the SC2 data set has roughly twice the bandwidth and more than an octave higher maximum frequency, as well as data at 10° lower grazing angles, than data sets considered in previous inversions at thick- and thin-mud sites (SWAMI and VC31-2, respectively) at the NEMP.<sup>13</sup>

The reflection-coefficient inversion at SC2 indicates an 11.7 m thick mud layer. The mud sound speed increases from the water-sediment interface to 2.4 m depth, remains essentially constant from 2.4 to 10.8 m, and increases rapidly to ~1700 m/s over 0.9 m to the mud-base interface (clearly resolved at 11.7 m depth). The sand-base interface is also well resolved, indicating an ~1.1 m thick layer with a mean sound speed of ~1735 m/s. This structure is consistent with a transition layer of increasing sand content in the mud above an underlying sand layer, as found in cores at thin-mud sites. An interface corresponding to the deep-base I reflector is indicated about 1.6 m below the sand. The attenuation profile indicates a slight decrease from 0 to 2.4 m depth and a clear increase from 10.8 to 11.7 m, which is, to our knowledge, the first such result for attenuation over the transition layer by inversion or direct measurement on the NEMP. The porosity profile is well estimated with values typical for mud to ~10.8 m depth and then transitions to sand values.

The geoacoustic profiles obtained here for SC2 provide significantly better structural resolution and smaller uncertainties compared with earlier results at SWAMI and VC31-2. This is likely because the angle and frequency ranges for the SC2 data include frequency-dependent critical-angle effects and Bragg oscillations, which are highly informative. To summarize a synthesis of the inversion results for SC2, SWAMI, and VC31-2:

- The sound-speed ratio at the water/sediment interface is found to be less than unity by an amount greater than the uncertainty at all sites.

- All sites indicate a small increase in sound speed over the upper layer of the mud, about 2–4 m thick. Below this, sound speed is essentially uniform down to about 1.1–1.3 m above the sand-base interface at the thick-mud sites (SC2 and SWAMI), but this intermediate mud layer is absent at the thin-mud site (VC31-2).
- At all sites, a transition layer exists in the lower mud over about 0.9–1.3 m above the sand layer over which the physical properties change rapidly with depth: Sound speed and density increase and porosity decreases. A monotonic increase in attenuation over the transition layer is clearly indicated in the high-quality inversion results at SC-2.
- All sites include a sand layer varying in thickness from 1.1 to 3.5 m below the transition layer, with relatively uniform properties over depth, including a sound speed of about 1740 m/s at the thick-mud sites and ~1800 m/s (but with higher uncertainty) at the thin-mud site.
- Apparent trends in sediment properties across site locations on the NEMP include the mud thickness increasing, the sand thickness and porosity decreasing, and the surficial sound speed and sound-speed ratio increasing in going from the northwest (VC31-2) to southeast (SC2).
- Within the full frequency bands considered in the three data sets (400–3125 Hz in all), there is no or very weak sound-speed dispersion in the mud layer, and the attenuation frequency dependence follows an approximately linear ( $f^1$ ) behavior.

The general sediment-column structure presented in this paper has also been observed in geoacoustic inversions of other types of data on the NEMP. For example, trans-D inversion of modal-dispersion data, including high-order modes (up to mode 21) at the SWAMI site, gave results similar to those obtained here.<sup>35</sup> The modal inversion results included a low surficial sound speed of approximately 1460 m/s, with a small increase in sound speed in the upper 4 m, followed by an iso-speed profile to about 8 m. From ~8 to 10.5 m, the sound speed increased from ~1480 to roughly 1800 m/s, representing the mud-to-sand transition, although with larger uncertainties and lower depth resolution than the reflection-coefficient inversions considered here. Other trans-D modal-dispersion inversions with smaller numbers of modes<sup>40,41</sup> at thick-mud sites (mud-base reflector at about 10 m) produced geoacoustic models with a low surficial sound speed, an iso-speed profile, and a transition from mud to sand sound speeds at a depth consistent with the mud-base reflector, but they do not resolve a sound-speed increase in the upper mud, likely due to more-limited data information content. Finally, trans-D inversion of ship-noise matched-field data<sup>42</sup> at a thinner-mud site (mud-base reflector at ~6 m) also produced a low surficial sound speed, iso-speed layer, and transition to higher speed at about the mud-base reflector, but with considerably higher uncertainties.

In summary, the compilation and synthesis of high-resolution reflection-coefficient inversion results at thick- and thin-mud sites on the NEMP developed here should

29 November 2023 23:25:25

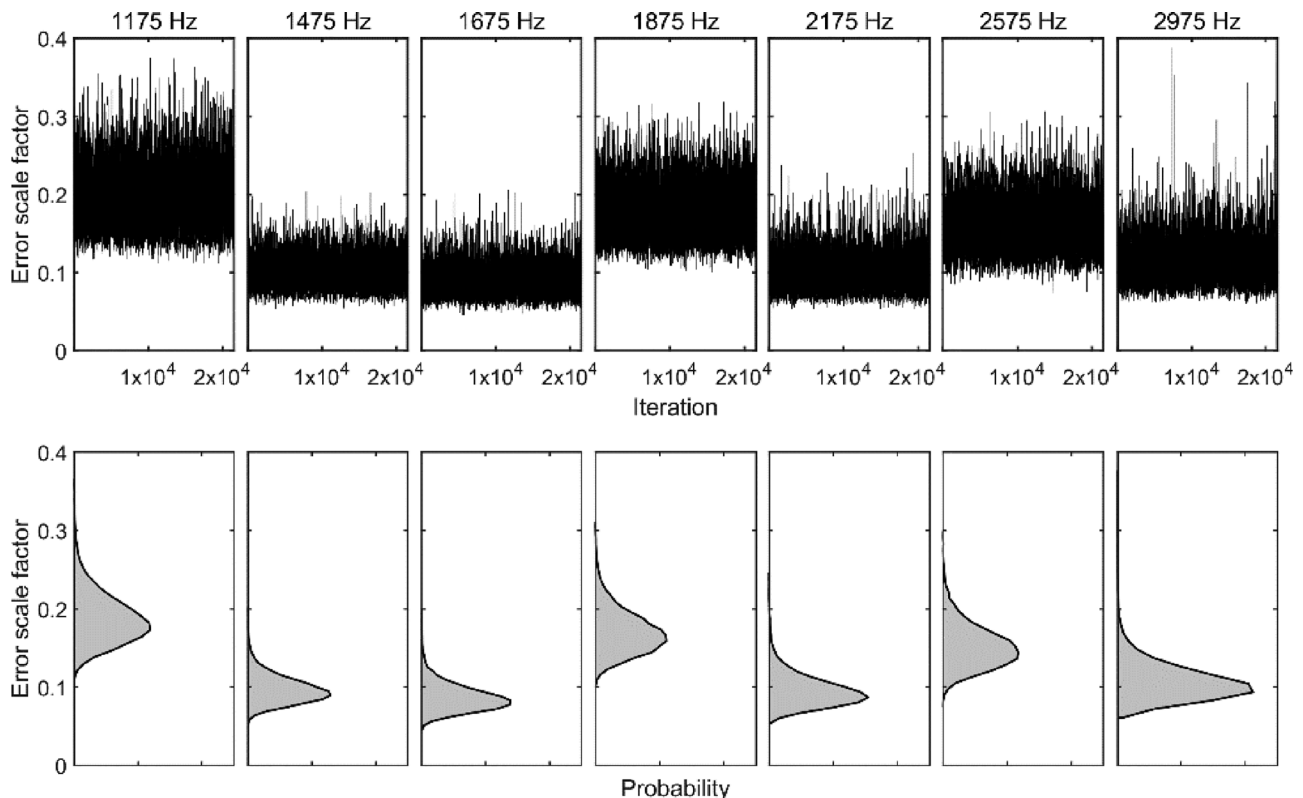


FIG. 11. Sampling histories and marginal probability densities for error scale factors at frequencies indicated.

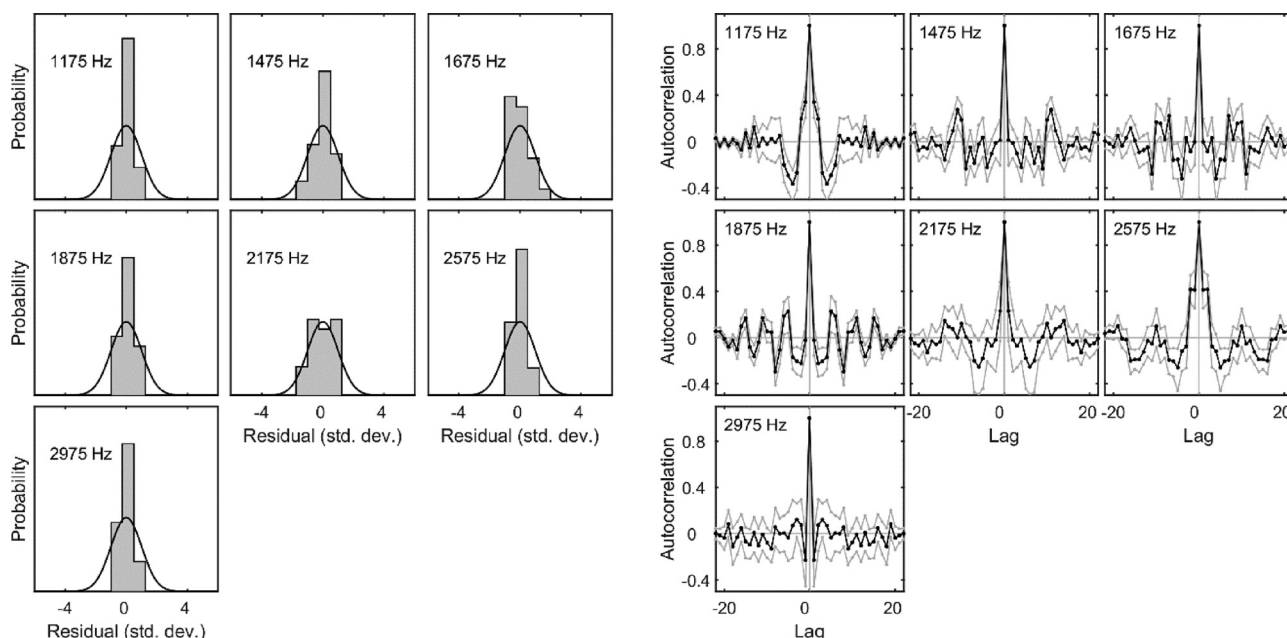


FIG. 12. Residual statistics. The histograms on the left show residual distributions compared to a standard Gaussian (black curves) at the frequencies indicated. The panels on the right show the mean residual autocorrelation functions (black dots and curves) and 95% CIs (gray dots and curves) for the ensemble of predicted data.

provide a useful model for sediment-column structure that can serve as a reference for and be refined by future work.

### ACKNOWLEDGMENT

This work was funded by the Office of Naval Research, Ocean Acoustics (322OA) program. The authors would like to thank J. Goff for providing chirp reflection survey data and the interpretation of the data and D. Knobles and P. Wilson for coordinating SBCEX17 activities.

### AUTHOR DECLARATIONS

#### Conflict of Interest

The authors have no conflicts of interest to disclose.

### DATA AVAILABILITY

The data that support the findings of this study are available from C.W.H. upon reasonable request.

### APPENDIX

This appendix examines the error model applied in the Bayesian geoacoustic inversion. This model was based on the assumption of uncorrelated Gaussian errors with the standard deviation at each frequency scaling directly with the data at that frequency, and the scale factor for each frequency treated as an unknown parameter in the inversion. The sampling histories and marginal probability densities from the inversion for these error scale factors are given in Fig. 11, which shows that the scale factors vary from about 0.1 to 0.2 (i.e., standard deviations are 10%–20% of the data values).

To consider the assumptions of Gaussian-distributed errors, Fig. 12 shows histograms of the error residuals (observed data minus predicted data sampled in the inversion), showing reasonable agreement compared to standard Gaussian distributions. In fact, the residuals for all frequencies except 2175 Hz pass the Kolmogorov–Smirnov test, indicating no evidence against the Gaussian assumption at the 0.05 level. Although the residuals at 2175 Hz did not pass this test, since the histogram is not strongly non-Gaussian (e.g., does not include large outliers), this is not a significant concern here.

To consider the assumption of uncorrelated errors, Fig. 12 also shows the residual autocorrelation function (means and 95% CI) at each frequency. Recognizing that the reflection-coefficient data are not uniformly spaced in angle, the autocorrelations nonetheless have narrow peaks,  $\approx 1$  lag-point wide at all frequencies except 2575 Hz, which is slightly wider. Further,  $>95\%$  of the samples at each frequency except 2575 Hz passed the runs test, indicating no evidence against the assumption of uncorrelated residuals at the 0.05 level, and at 2575 Hz,  $\sim 60\%$  of samples passed. Hence, the assumption of uncorrelated errors appears to be well supported.

- <sup>1</sup>M. D. Collins, W. A. Kuperman, and H. Schmidt, “Nonlinear inversion for ocean-bottom properties,” *J. Acoust. Soc. Am.* **92**, 2770–2783 (1992).
- <sup>2</sup>S. E. Dosso, M. L. Yeremy, J. M. Ozard, and N. R. Chapman, “Estimation of ocean-bottom properties by matched-field inversion of acoustic field data,” *IEEE J. Ocean. Eng.* **18**, 232–239 (1993).
- <sup>3</sup>P. Gerstoft, “Inversion of acoustic data using a combination of genetic algorithms and the Gauss–Newton approach,” *J. Acoust. Soc. Am.* **97**, 2181–2190 (1995).
- <sup>4</sup>Z.-H. Michalopoulou, “Matched-impulse-response processing for shallow-water localization and geoacoustic inversion,” *J. Acoust. Soc. Am.* **108**, 2082–2090 (2000).



- <sup>5</sup>D. P. Knobles, R. A. Koch, L. A. Thompson, K. C. Focke, and P. E. Eisman, "Broadband sound propagation in shallow water and geoacoustic inversion," *J. Acoust. Soc. Am.* **113**, 205–222 (2003).
- <sup>6</sup>S. E. Dosso, P. L. Nielsen, and M. J. Wilmut, "Data error covariance in matched-field geoacoustic inversion," *J. Acoust. Soc. Am.* **119**, 208–219 (2006).
- <sup>7</sup>J. Dettmer, S. E. Dosso, and C. W. Holland, "Full wave-field reflection coefficient inversion," *J. Acoust. Soc. Am.* **122**, 3327–3337 (2007).
- <sup>8</sup>J. Dettmer, S. E. Dosso, and C. W. Holland, "Joint time/frequency-domain inversion of reflection data for seabed geoacoustic profiles and uncertainties," *J. Acoust. Soc. Am.* **123**, 1306–1317 (2008).
- <sup>9</sup>C. W. Holland, "Geoacoustic inversion for fine-grained sediments," *J. Acoust. Soc. Am.* **111**, 1560–1564 (2002).
- <sup>10</sup>C. W. Holland and J. Osler, "High-resolution geoacoustic inversion in shallow water: A joint time- and frequency-domain technique," *J. Acoust. Soc. Am.* **107**, 1263–1279 (2000).
- <sup>11</sup>C. W. Holland, C. M. Smith, Z. Lowe, and J. Dorminy, "Seabed observations at the New England Mud Patch: Reflection and scattering measurements and direct geoacoustic information," *IEEE J. Ocean. Eng.* **47**, 578–593 (2022).
- <sup>12</sup>P. S. Wilson, D. P. Knobles, and T. A. Neilsen, "Guest editorial: An overview of the seabed characterization experiment," *IEEE J. Ocean. Eng.* **45**, 1–13 (2020).
- <sup>13</sup>J. Belcourt, C. W. Holland, S. E. Dosso, and J. Dettmer, "Depth-dependent geoacoustic interferences with dispersion at the New England Mud Patch via reflection coefficient inversion," *IEEE J. Ocean. Eng.* **45**, 69–91 (2020).
- <sup>14</sup>C. W. Holland and S. E. Dosso, "On compressional wave attenuation in muddy marine sediments," *J. Acoust. Soc. Am.* **149**, 3674–3687 (2021).
- <sup>15</sup>J. A. Goff, A. H. Reed, G. Gawarkiewicz, P. S. Wilson, and D. P. Knobles, "Stratigraphic analysis of a sediment pond within the New England Mud Patch: New constraints from high-resolution chirp acoustic reflection data," *Mar. Geol.* **412**, 81–94 (2019).
- <sup>16</sup>J. D. Chaytor, M. S. Ballard, B. J. Buczkowski, J. A. Goff, K. M. Lee, A. H. Reed, and A. A. Boggess, "Measurements of geologic characteristics and geophysical properties of sediments from the New England Mud Patch," *IEEE J. Ocean. Eng.* **47**, 503–530 (2022).
- <sup>17</sup>J. Belcourt, S. E. Dosso, C. W. Holland, and J. Dettmer, "Linearized Bayesian inversion for experiment geometry at the New England Mud Patch," *IEEE J. Ocean. Eng.* **45**, 60–68 (2020).
- <sup>18</sup>M. J. Buckingham, "On pore-fluid viscosity and the wave properties of saturated granular materials including marine sediments," *J. Acoust. Soc. Am.* **122**, 1486–1501 (2007).
- <sup>19</sup>C. W. Holland and J. Dettmer, "In situ sediment dispersion estimates in the presence of discrete layers and gradients," *J. Acoust. Soc. Am.* **133**, 50–61 (2013).
- <sup>20</sup>C. W. Holland, P. L. Nielsen, J. Dettmer, and S. E. Dosso, "Resolving meso-scale seabed variability using reflection measurements from an autonomous underwater vehicle," *J. Acoust. Soc. Am.* **131**, 1066–1078 (2012).
- <sup>21</sup>J. Dettmer, C. W. Holland, and S. E. Dosso, "Trans-dimensional uncertainty estimation for dispersive seabed sediments," *Geophysics* **78**, WB63–WB76 (2013).
- <sup>22</sup>F. B. Jensen, W. A. Kuperman, M. B. Porter, and H. Schmidt, *Computational Ocean Acoustics* (Springer, New York, 1994), pp. 1–794.
- <sup>23</sup>D. Levin, "Fast integration of rapidly oscillatory functions," *J. Comput. Appl. Math.* **67**, 95–101 (1996).
- <sup>24</sup>J. E. Quijano, S. E. Dosso, J. Dettmer, and C. W. Holland, "Fast computation of seabed spherical-wave reflection coefficients in geoacoustic inversion," *J. Acoust. Soc. Am.* **138**, 2106–2117 (2015).
- <sup>25</sup>P. J. Green, "Trans-dimensional Markov chain Monte Carlo," in *Highly Structured Stochastic Systems* (Oxford University, New York, 2003), pp. 179–198.
- <sup>26</sup>J. Dettmer, S. E. Dosso, and C. W. Holland, "Trans-dimensional geoacoustic inversion," *J. Acoust. Soc. Am.* **128**, 3393–3405 (2010).
- <sup>27</sup>S. E. Dosso, J. Dettmer, G. Steininger, and C. W. Holland, "Efficient trans-dimensional Bayesian inversion for geoacoustic profile estimation," *Inverse Probl.* **30**, 114018–114029 (2014).
- <sup>28</sup>P. J. Green, "Reversible jump Markov chain Monte Carlo computation and Bayesian model determination," *Biometrika* **82**, 711–732 (1995).
- <sup>29</sup>D. J. Earl and M. W. Deem, "Parallel tempering: Theory, applications, and new perspectives," *Phys. Chem. Chem. Phys.* **7**, 3910–3916 (2005).
- <sup>30</sup>A. Jasra, D. A. Stephens, and C. C. Holmes, "Population-based reversible jump Markov chain Monte Carlo," *Biometrika* **94**, 787–807 (2007).
- <sup>31</sup>S. E. Dosso, C. W. Holland, and M. Sambridge, "Parallel tempering in strongly nonlinear geoacoustic inversion," *J. Acoust. Soc. Am.* **132**, 3030–3040 (2012).
- <sup>32</sup>S. E. Dosso and M. J. Wilmut, "Uncertainty estimation in simultaneous Bayesian tracking and environmental inversion," *J. Acoust. Soc. Am.* **124**, 82–97 (2008).
- <sup>33</sup>D. R. Jackson and M. D. Richardson, *High-Frequency Seafloor Acoustics* (Springer, New York, 2007), pp. 114–188.
- <sup>34</sup>M. D. Richardson, "In-situ, shallow-water sediments geoacoustic properties," in *Shallow Water Acoustics*, edited by R. Zhang and J.-X. Zhou (China Ocean, Beijing, 1997), pp. 163–170.
- <sup>35</sup>S. E. Dosso and J. Bonnel, "Hybrid seabed parameterization to investigate geoacoustic gradients at the New England Mud Patch," *IEEE J. Ocean. Eng.* **47**, 620–634 (2022).
- <sup>36</sup>T. J. Gorgas, R. H. Wilkens, S. S. Fu, L. N. Frazer, M. D. Richardson, K. B. Briggs, and H. Lee, "In situ acoustic and laboratory ultrasonic sound speed and attenuation measured in heterogeneous soft seabed sediments: Eel River shelf, California," *Mar. Geol.* **182**, 103–119 (2002).
- <sup>37</sup>J. Yang and D. R. Jackson, "Measurement of sound speed in fine-grained sediments during the seabed characterization experiment," *IEEE J. Ocean. Eng.* **45**, 39–50 (2020).
- <sup>38</sup>D. P. Knobles, C. D. Escobar-Amado, M. J. Buckingham, W. S. Hodgkiss, and P. S. Wilson, "Statistical inference of sound speed and attenuation dispersion of a fine-grained marine sediment," *IEEE J. Ocean. Eng.* **47**, 553–564 (2022).
- <sup>39</sup>L. Wan, M. Badiy, D. P. Knobles, P. S. Wilson, and J. Goff, "Estimates of low-frequency sound speed and attenuation in a surface mud layer using low-order modes," *IEEE J. Ocean. Eng.* **45**, 201–211 (2020).
- <sup>40</sup>Y.-M. Jiang, S. E. Dosso, J. Bonnel, P. S. Wilson, and D. P. Knobles, "Passive acoustic glider for seabed characterization at the New England Mud Patch," *IEEE J. Ocean. Eng.* **47**, 541–552 (2022).
- <sup>41</sup>J. Bonnel, S. E. Dosso, D. Eleftherakis, and N. R. Chapman, "Trans-dimensional inversion of modal dispersion data on the New England Mud Patch," *IEEE J. Ocean. Eng.* **45**, 116–130 (2020).
- <sup>42</sup>D. Tollefsen, S. E. Dosso, and D. P. Knobles, "Ship-of-opportunity noise inversions for geoacoustic profiles of a layered mud-sand seabed," *IEEE J. Ocean. Eng.* **45**, 189–200 (2020).